

This is a repository copy of *Spectral broadening from turbulence in multiscale lower hybrid current drive simulations*.

White Rose Research Online URL for this paper:

<https://eprints.whiterose.ac.uk/195090/>

Version: Published Version

Article:

Biswas, Bodhi orcid.org/0000-0001-7993-3732, Bonoli, Paul, Ram, Abhay et al. (1 more author) (2022) Spectral broadening from turbulence in multiscale lower hybrid current drive simulations. Nuclear Fusion. 016029. ISSN 1741-4326

<https://doi.org/10.1088/1741-4326/aca6fb>

Reuse

This article is distributed under the terms of the Creative Commons Attribution (CC BY) licence. This licence allows you to distribute, remix, tweak, and build upon the work, even commercially, as long as you credit the authors for the original work. More information and the full terms of the licence here:

<https://creativecommons.org/licenses/>

Takedown

If you consider content in White Rose Research Online to be in breach of UK law, please notify us by emailing eprints@whiterose.ac.uk including the URL of the record and the reason for the withdrawal request.

PAPER • OPEN ACCESS

Spectral broadening from turbulence in multiscale lower hybrid current drive simulations


To cite this article: Bodhi Biswas *et al* 2023 *Nucl. Fusion* **63** 016029

View the [article online](#) for updates and enhancements.

You may also like

- [Robust real-time feedback algorithms for plasma kinetic control in advanced tokamak scenarios](#)
S Wang, D Moreau, E Witrant et al.
- [Progress towards steady-state regimes in Alcator C-Mod](#)
S. Shiraiwa, G. Baek, P.T. Bonoli et al.
- [Comparative modelling of lower hybrid current drive with two launcher designs in the Tore Supra tokamak](#)
E. Nilsson, J. Decker, Y. Peysson et al.

Spectral broadening from turbulence in multiscale lower hybrid current drive simulations

Bodhi Biswas^{a,*} , Paul Bonoli, Abhay Ram and Anne White

Plasma Science and Fusion Center, Massachusetts Institute of Technology, Cambridge, MA, United States of America

E-mail: bodhi.biswas@york.ac.uk

Received 6 October 2022, revised 22 November 2022

Accepted for publication 29 November 2022

Published 16 December 2022



CrossMark

Abstract

The scattering of lower hybrid (LH) waves due to scrape-off layer filaments is investigated. It is revealed that scattering can account for the LH spectral gap without any ad hoc modification to the wave-spectrum. This is shown using a multiscale simulation approach which allows, for the first time, the inclusion of full-wave scattering physics in ray-tracing/Fokker–Planck calculations. In this approach, full-wave scattering probabilities are calculated for a wave interacting with a statistical ensemble of filaments. These probabilities are coupled to ray-tracing equations using radiative transfer theory. This allows the modeling of scattering along the entire ray-trajectory, which can be important in the multi-pass regime. Simulations are conducted for LH current drive (LHCD) in Alcator C-Mod, resulting in excellent agreement with experimental current and hard x-ray profiles. A region in filament parameter space is identified in which the impact of scattering on LHCD is saturated. Such a state coincides with experimental LHCD measurements, suggesting saturation indeed occurs in C-Mod, and therefore the exact statistical properties of the filaments are not important.

Keywords: LHCD, filament, Alcator C-Mod, turbulence

(Some figures may appear in colour only in the online journal)

1. Introduction

Lower hybrid waves are an efficient means to non-inductively drive current in a tokamak via electron Landau damping (ELD) [1]. It is an attractive actuator for current profile shaping, which has been successfully demonstrated in several tokamaks [2–6]. There is also interest in targeted LHCD for neoclassical tearing mode suppression [7, 8].

The condition for strong linear ELD is [9]

$$|N_{||}| \geq N_{||,\text{ELD}} \equiv \frac{c}{3v_{te}} \quad (1)$$

where $N_{||} \equiv \mathbf{N} \cdot \mathbf{B}/B$ is the parallel refractive index (with respect to the background magnetic field \mathbf{B}), c is the speed of light, and $v_{te} = \sqrt{2T_e/m_e}$ is electron thermal velocity (with T_e and m_e being the electron temperature and mass, respectively). If the initial parallel refractive index $|N_{||0}| < N_{\text{ELD}}$, the wave is expected to first undergo $|N_{||}|$ -upshift due to toroidicity until the condition in equation (1) is met [10]. For a sufficiently large *spectral-gap* between $|N_{||0}|$ and N_{ELD} , the wave may require multiple passes through the plasma before this gap is bridged. This scenario is typical of present-day tokamaks due to low core T_e .

A large spectral-gap poses difficulties for theory and modeling of LHCD. Ray-tracing/Fokker–Planck modeling of

^a Present affiliation: University of York, United Kingdom of Great Britain and Northern Ireland.

* Author to whom any correspondence should be addressed.



Original Content from this work may be used under the terms of the [Creative Commons Attribution 4.0 licence](https://creativecommons.org/licenses/by/4.0/). Any further distribution of this work must maintain attribution to the author(s) and the title of the work, journal citation and DOI.

LHCD reveal large discrepancies between simulations and experiments in several tokamaks [11–14]. In high aspect ratio devices ($\mathcal{A} \equiv R_0/a \gtrsim 5$, where R_0 is the major radius, and a is the minor radius), like WEST and TRIAM-1, toroidicity is insufficient to bridge the spectral-gap via $|N_{||}|$ -upshift. In moderate aspect ratio devices ($\mathcal{A} \approx 3$), like Alcator C-Mod and EAST, toroidicity can accurately model the *total* current drive efficiency, but not the radial current or hard x-ray (HXR) profiles [11, 13]. For example, in C-Mod, the simulated LH current profiles are not smooth and are peaked far off-axis, while experimental motional Stark effect (MSE) and HXR measurements suggest smooth profiles robustly peaked on-axis [11]. Consequently, $N_{||}$ -upshift due to toroidicity is not adequate for understanding experimental observations. There exist other contributing factors that must be taken into account in theoretical models.

Several mechanisms have been proposed as possible explanations for the spectral gap. Ad hoc modifications to the launched LH wave-spectrum reveal that either $N_{||}$ broadening [15] or angle-broadening of the perpendicular refractive index (N_{\perp}) [16] can explain experimental current drive results in C-Mod.

The two theorized causes of $N_{||}$ broadening are parametric decay instabilities (PDI) [17, 18] and scattering from parallel density fluctuations in front of the LH antenna [19]. In FTU, a combination of modeling and experiment shows PDI is likely responsible for low LHCD efficiency at high densities [20, 21]. However, there is little theoretical support for—or experimental evidence of—strong PDI in low and moderate density C-Mod discharges ($\bar{n}_e < 10^{20} \text{ m}^{-3}$) where the spectral gap persists [22]. Likewise, there is little evidence of density fluctuations with the large parallel gradients required to induce a significant $N_{||}$ -broadening.

The most likely mechanism for N_{\perp} angle-broadening is scattering from turbulent scrape-off layer (SOL) fluctuations. Prior models have employed either ray-tracing [23, 24] or wave-kinetic treatments [10, 25, 26] for scattering in drift-wave turbulence. These models have demonstrated modified current profiles, but cannot match experimental observations. Gas-puff imaging (GPI) [27] and statistical analysis of Langmuir probe measurements [28] in the SOL have motivated the modeling of LH scattering from intermittent, field-aligned filaments. The extent of N_{\perp} angle-broadening from filaments is greater than in ‘equivalent’ drift-wave turbulence [29]. A recent hybrid full-wave/statistical model for wave–filament interactions was developed to model the modification to the LH wave-spectrum in front of the antenna [30]. Multiple wave–filament interactions are accounted for using the radiative transfer (RT) equation. This treatment allows the modeling of realistic turbulence parameters without being restricted to the validity constraints of the ray-tracing or random phase approximation. The study finds a large angle-broadening of the incident wave-spectrum, enough to robustly direct a fraction of LH power to damp on-axis on first pass through the plasma. In turn, the LH current profile is monotonic and peaked on-axis, in much closer agreement with experiment. In addition, asymmetric scattering of the LH wave is observed in angle-space. This is a full-wave effect only possible with intermittent

density fluctuations, and therefore is not accounted for in prior ray-tracing or wave-kinetic treatments.

The hybrid full-wave/statistical scattering model discussed above is limited to a slab geometry with homogeneous background and turbulence parameters. It also only treats slow wave to slow wave ($S \rightarrow S$) scattering and ignores the fast (F) wave. Therefore this model can only approximately treat scattering directly in front of the LH antenna. In this paper, the more general RT equation is solved using a multiscale full-wave/ray-tracing solver. It allows the modeling of arbitrary geometry and both like-mode ($S \rightarrow S$, $F \rightarrow F$) and unlike-mode ($S \rightarrow F$, $F \rightarrow S$) scatter. An arbitrary geometry allows accounting for realistically tapered SOL turbulence profiles in a tokamak, and models scattering along the entire ray-trajectory (important in the multi-pass regime). The inclusion of all scattering modes is especially important near the mode-conversion density where like- and unlike-mode scattering probabilities are comparable.

This multiscale model is applied to Alcator C-Mod, allowing, for the first time, the inclusion of self-consistent full-wave scattering physics in LHCD simulations. The resulting current and HXR profiles provide excellent matches to experimental measurements. Thus, the spectral-gap in C-Mod is resolved via turbulent scattering, and without any ad hoc modification to the wave-spectrum.

This paper is organized as follows. Section 2 will describe the multiscale scattering model. Section 3 discusses its application to LHCD in Alcator C-Mod discharges. Section 4 provides a discussion and summary of the findings.

2. Multiscale scattering model

From a modeling perspective, the LH wave is in an interesting and challenging range of wavelengths. The wavelength is small enough to employ ray-tracing in the quiescent core [31], but large enough that full-wave modeling is required for common SOL turbulence parameters. On the other hand, the LH wavelength is small enough such that whole-device full-wave modeling in a turbulent plasma is prohibitively expensive. Therefore, a multiscale model that employs ray-tracing in the core and a full-wave solver in the SOL is a promising concept. The implementation is as follows. A Mie-scattering approach efficiently calculates the scattering probabilities for an incident plane wave interacting with a filament. The probabilities are averaged over a statistical ensemble of filament parameters. Next, the scattering of RF power in phase-space is modeled using the RT approximation. The RT equation is solved in a ray-tracing solver, where the scattering terms act as stochastic kicks to the ray-trajectory. Finally, the rays are used to calculate current drive using the quasi-linear Fokker–Planck equation.

2.1. Review of single wave–filament interaction

The Mie-scattering model for a single wave–filament interaction is briefly reviewed. An incident LH plane wave, either the slow (S) or fast (F) mode, travels through a cold magnetized

plasma with a homogeneous background density n_0 and magnetic field \mathbf{B} . The magnetic field is aligned along $\hat{\mathbf{e}}_z$, such that the parallel wave-number $k_{\parallel} = k_z$. The wave trajectory is aligned such that $\mathbf{v}_{gr\perp} = v_{gr\perp} \hat{\mathbf{e}}_x$, where $\mathbf{v}_{gr\perp}$ is the perpendicular group velocity and $v_{gr\perp} > 0$. An infinitely long, cylindrical, field-aligned filament passes through the origin with density n_b . Given this is a poloidally symmetric system (where $\theta = \tan^{-1}(y/x)$), the Jacobi–Anger expansion is used to write the electric field in cylindrical coordinates (ρ, θ, z) . Consequently, the field everywhere is a series solution in poloidal mode-numbers ($m \equiv k_{\theta}\rho$),

$$E_{j\beta} = e^{i(k_{\parallel}z - \omega t)} \sum_{m=-\infty}^{+\infty} E_{jm} W_{j\beta m} e^{im\theta}; \quad \beta = \rho, \theta, z \quad (2a)$$

$$W_{j\rho m} = \xi_{jx} J'_m(k_{j\perp}\rho) - i\xi_{jy} \frac{m}{k_{j\perp}\rho} J_m(k_{j\perp}\rho) \quad (2b)$$

$$W_{j\theta m} = i\xi_{jx} \frac{m}{k_{j\perp}\rho} J_m(k_{j\perp}\rho) + \xi_{jy} J'_m(k_{j\perp}\rho) \quad (2c)$$

$$W_{jz m} = i\xi_{jz} J_m(k_{j\perp}\rho) \quad (2d)$$

where $j = 0, \dots, 4$ is the wave index, indicating (0) the incident wave, (1, 2) the slow/fast mode inside the filament, and (3, 4) the slow/fast mode outside the filament. $\bar{\xi}_j = \{\xi_{jx}, \xi_{jy}, \xi_{jz}\}$ is the plane-wave polarization of wave j . J_m is the Bessel function of the first kind and order m . J'_m is the first derivative of J_m with respect to its argument. The coefficients E_{jm} for the incident plane wave ($j=0$) are known through the Jacobi–Anger expansion. The coefficients for the remaining waves are found by imposing Maxwell's boundary conditions at the filament perimeter. This is detailed in Ram and Hizanidis [32].

This technique can be extended to a radially varying filament density profile, as detailed in Biswas *et al* [30]. A similar method was used to model ion-cyclotron wave scattering [33]. For the purposes of this work, it is assumed the filament has a Gaussian density profile such that

$$n(\rho) - n_0 = n_0 \left(\frac{n_b}{n_0} - 1 \right) e^{-\left(\frac{2\sqrt{\ln(2)}\rho}{a_b} \right)^2} \quad (3)$$

where n is the density, n_b/n_0 is the relative density of the filament, and a_b is the full-width half max of the filament radial profile.

Following [30, 34], the differential scattering-width is calculated by evaluating the radially scattered Poynting flux in the far-field limit

$$\sigma_{j \rightarrow j'}(\theta) = \frac{\mp 2 \left[|\xi_{j'y}|^2 + |\xi_{j'z}|^2 + \frac{k_z}{k_{j'\perp}} \text{Re}\{\xi_{j'x}\xi_{j'z}^*\} \right]}{\pi \left[k_{jx} (|\xi_{jy}|^2 + |\xi_{jz}|^2) - k_z \text{Re}\{\xi_{jx}\xi_{jz}^*\} \right]} \times \left| \sum_{m=-\infty}^{+\infty} i^{\pm m} E_{j'm} e^{im\theta} \right|^2 \quad (4)$$

where now $j = S, F$ is the incident mode, j' is the scattered mode, $\xi_{j\ell}$ is the ℓ -component of the electric field polarization of mode j , and $k_{j\ell}$ is the ℓ -component of the wave-number of mode j . The sign \mp depends on the scattered mode.

The differential scattering-width is analogous to a differential scattering cross-section. Likewise, $\sigma = \int \sigma(\theta) d\theta$ is the scattering-width, which is analogous to a scattering cross-section. Lastly, $\hat{\sigma}(\theta) \equiv \sigma(\theta)/\sigma$ is the normalized differential scattering-width and will be useful in writing the RT equation.

Note that, within this full-wave model, the plasma is assumed loss-less. (Collisional and Landau damping of scattered waves is accounted for in the ray-tracer, as will be described in section 2.3.) One consequence is that the right-hand side of equation (4) is zero for $k_{j'\perp}^2 < 0$. In addition, any parasitic losses of evanescent scattered modes or bound modes within the filament are neglected in this analysis. This loss mechanism is theorized to be important during high harmonic fast wave launch [35].

2.2. Scattering through statistical ensemble of filaments

To account for the statistical variation in filament relative density (n_b/n_0) and radial width (a_b), a joint probability distribution function $p(n_b/n_0, a_b)$ is defined for an ensemble of filaments. The quantities $\langle n_b/n_0 \rangle$ and $\langle a_b \rangle$ denote the average relative density and radial width of filaments. The average, or 'effective', differential scattering-width is

$$\sigma_{\text{eff}, j \rightarrow j'}(\theta) = \langle \sigma_{j \rightarrow j'}(\theta) \rangle = \int_0^{\infty} da_b \int_0^{\infty} d(n_b/n_0) \sigma_{j \rightarrow j'}(\theta; n_b/n_0, a_b) p(n_b/n_0, a_b). \quad (5)$$

A wave packet traveling in a straight line will encounter, on average, $\frac{f_p}{\pi \langle a_b \rangle^2}$ filaments per unit length in the perpendicular plane. Thus, the inverse mean-free-path to scatter is

$$\Sigma_{\text{eff}, j \rightarrow j'} = \frac{f_p}{\pi \langle a_b \rangle^2} \sigma_{\text{eff}, j \rightarrow j'} \quad (6)$$

where f_p is the packing-fraction, which is defined as the fractional area (in the perpendicular plane) inhabited by filaments. Note that $\Sigma_{\text{eff}, j \rightarrow j'}$ and $\sigma_{\text{eff}, j \rightarrow j'}(\theta)$ are dependent on the local plasma parameters, the incident wave's frequency and wavenumber, and the filament PDF. These functional dependencies are only stated explicitly when needed.

2.3. RT approximation

RT theory models the RF wave-spectrum as a wave-packet distribution function in phase-space, akin to the Fokker–Planck equation for a particle distribution function [25]. We define $P_j(\mathbf{r}, \mathbf{k})$ as the distribution corresponding to the LH mode j . The RT equation governing P_j is

$$\left(\frac{dP_j}{dt} \right)_r + 2\gamma(\mathbf{k}_j, \mathbf{r}) P_j = \left(\frac{dP_j}{dt} \right)_{\text{sc}}. \quad (7)$$

The $(\dots)_r$ term is the convective term accounting for the trajectory for a wave-packet/ray. The second term accounts for wave damping, where γ is the damping rate. The left hand side (LHS) is routinely solved using ray-tracing/Fokker–Planck codes. The right hand term accounts for the added effect of scattering,

$$\begin{aligned}
\left(\frac{dP_j}{dt}\right)_{\text{sct}} &= \sum_{j'=S,F} -\Sigma_{\text{eff},j \rightarrow j'}(k_{\parallel}, \mathbf{r}) |\mathbf{v}_{gr\perp}(\mathbf{k}_j, \mathbf{r})| P_j \\
&+ \sum_{j'=S,F} \Sigma_{\text{eff},j' \rightarrow j}(k_{\parallel}, \mathbf{r}) |\mathbf{v}_{gr\perp}(\mathbf{k}_{j'}, \mathbf{r})| \\
&\times \int_{-\pi}^{\pi} \tilde{\sigma}_{\text{eff},j' \rightarrow j}(\chi - \chi'; k_{\parallel}, \mathbf{r}) P_{j'}(\chi', k_{\parallel}, \mathbf{r}) d\chi'.
\end{aligned} \tag{8}$$

The transformation of $\theta \rightarrow \chi$ must first be explained. The variable θ describes the angle of scatter in the frame of a single filament-wave interaction, as described in section 2.1. In contrast, χ is defined through $\mathbf{b} \cdot (\hat{\mathbf{e}}_{\psi} \times \mathbf{k}_{\perp}) = k_{\perp} \sin \chi$, where $\hat{\mathbf{e}}_{\psi}$ is the unit vector normal to the flux surface and directed outwards, and $\mathbf{b} \equiv \mathbf{B}/B$ is the unit vector along the magnetic field. Thus, by using χ , the angular orientation of \mathbf{k}_{\perp} is unambiguously defined in a tokamak geometry. The functional dependence of $P_j(\mathbf{r}, \mathbf{k})$ can be mapped to $P_j(\chi, k_{\parallel}, \mathbf{r})$ and vice-versa using the dispersion relation for the appropriate mode, and the local magnetic geometry.

The two right hand side (RHS) terms in equation (8) account for angular (χ) rotation of the perpendicular wave-vector \mathbf{k}_{\perp} due to a wave–filament interaction. The first term accounts for *out-scatter* of P_j from a phase-space volume element centered at χ . The second term accounts for *in-scatter* into this volume element from all other angles χ' . Note that the scattering probabilities and background plasma parameters are allowed to vary in real-space. In addition, the summation over the slow and fast modes now ensure that both like-mode and unlike-mode scatter ($S \rightarrow F, F \rightarrow S$) are accounted for. In contrast, the system studied in [30] was restricted to homogeneous scattering and background parameters, and neglected mode-conversion.

It should be clarified that, in generating scattering probabilities using a full-wave formalism, interference effects during a single wave–filament interaction are accounted for. However, in using the RT approximation, the interference effects of simultaneous multi-filament scattering are ignored. This is a reasonable approximation as long as $k_{\perp} d \gg 1$, where d is the average distance between filaments [36]. Code comparison with a fully numeric full-wave solver finds that this multiscale method generally overestimates the effects of scattering for $f_p \gtrsim 0.15$ [30]. In addition, ray-tracing is only valid for $k_{\perp} L_{\perp} \gg 1$, where L_{\perp} is the perpendicular length scale on the plasma. This poses a problem near the LH cut-off ($\omega_{pe}/\omega \rightarrow 1$, where ω_{pe} is the electron plasma frequency) because $k_{\perp} \rightarrow 0$. In the multi-pass regime, rays commonly reflect at the cutoff in the far-SOL. Thus, the use of ray-tracing in this narrow region is not strictly accurate, and any conclusions about scattering are affected by this inconsistency. Nevertheless, the multiscale model retains many important full-wave effects and is therefore a significant improvement over prior reduced RF-turbulence scattering models in the SOL.

2.4. Coupling to ray-tracing code GENRAY

The initial wave-spectrum, launched from the LH antenna, is discretized into rays. Each ray-trajectory is evolved using

the ray-tracing equations in GENRAY [37]. The quasi-linear calculation of γ , accounting for Landau damping and collisions, is accomplished with the Fokker–Planck solver CQL3D [38]. In this way, the usual ray-tracing/Fokker–Planck calculation solves for the LHS of equation (7).

The RHS of equation (7) introduces stochastic kicks to the ray-trajectories via a Monte Carlo process. Previous ray-tracing Monte Carlo scattering models exist for drift-wave turbulence [10, 26]. In GENRAY, after one time-step of Δt , the ray-trajectory is evolved from \mathbf{r} to $\mathbf{r} + \Delta \mathbf{r}$, where \mathbf{r} is a spatial coordinate and $\Delta \mathbf{r} = \mathbf{v}_{gr} \Delta t$. Given $\Sigma_{\text{eff},j \rightarrow j'}$ is the inverse mean free path for like-mode scatter, the probability of this scattering event during this time-step is $p_{\text{sct}} = 1 - e^{-\Sigma_{\text{eff},j \rightarrow j'} |\Delta \mathbf{r}_{\perp}|} \approx \Sigma_{\text{eff},j \rightarrow j'} |\Delta \mathbf{r}_{\perp}|$, where $|\Delta \mathbf{r}_{\perp}|$ is the distance travelled perpendicular to \mathbf{b} . The approximation holds for $\Sigma_{\text{eff},j \rightarrow j'} |\Delta \mathbf{r}_{\perp}| \ll 1$. The probability of unlike-mode scatter, and no scatter, are calculated in a similar manner. After each time-step, a uniformly distributed random variable $X_1 \in [0, 1]$ is sampled. Assuming the incident ray is a slow wave, there are three possibilities,

- $X_1 < \Sigma_{\text{eff},S \rightarrow S} |\Delta \mathbf{r}_{\perp}|$. Then a $S \rightarrow S$ scatter occurs.
- $\Sigma_{\text{eff},S \rightarrow S} |\Delta \mathbf{r}_{\perp}| \leq X_1 < (\Sigma_{\text{eff},S \rightarrow S} + \Sigma_{\text{eff},S \rightarrow F}) |\Delta \mathbf{r}_{\perp}|$. Then a $S \rightarrow F$ scatter occurs.
- $X_1 \geq (\Sigma_{\text{eff},S \rightarrow S} + \Sigma_{\text{eff},S \rightarrow F}) |\Delta \mathbf{r}_{\perp}|$. Then no scatter occurs.

The above stochastic scattering procedure is only valid when the scattering probability between time-steps is small ($(\Sigma_{\text{eff},S \rightarrow S} + \Sigma_{\text{eff},S \rightarrow F}) |\Delta \mathbf{r}_{\perp}| \ll 1$). Once a scattering event is initiated, another uniformly distributed random variable $X_2 \in [0, 1]$ is sampled. A new variable is introduced:

$$\tilde{\sigma}_{\text{eff},j \rightarrow j'}(\chi) = \frac{1}{\sigma_{\text{eff},j \rightarrow j'}} \int_{-\pi}^{\chi} \sigma_{\text{eff},j \rightarrow j'}(\chi') d\chi' \tag{9}$$

where $\tilde{\sigma}_{\text{eff},j \rightarrow j'}(\Delta \chi)$ is the cumulative distribution function (CDF) of rotating the incident ray \mathbf{k}_{\perp} by angle $\Delta \chi$. Inversely,

$$\Delta \chi = \tilde{\sigma}_{\text{eff},j \rightarrow j'}^{-1}(X_2). \tag{10}$$

Therefore, the incident ray is converted to a scattered ray, by first undergoing mode-conversion in the case of unlike-mode scatter, and then rotating $\mathbf{v}_{gr\perp}$ by $\Delta \chi$ with respect to \mathbf{b} . Note that, in the case of like-mode scatter, this is equivalent to rotating \mathbf{k}_{\perp} by $\Delta \chi$. In the case of unlike-mode scatter, the direction of \mathbf{k}_{\perp} is rotated by $\Delta \chi + \pi$ because the fast wave is forward-propagating ($\mathbf{k}_{\perp} \cdot \mathbf{v}_{gr\perp} = |k_{\perp} v_{gr\perp}|$) while the slow wave is backward-propagating ($\mathbf{k}_{\perp} \cdot \mathbf{v}_{gr\perp} = -|k_{\perp} v_{gr\perp}|$).

The Monte Carlo scattering model, as described above, can also account for an incident fast wave in a similar manner. Thus the scattering of both slow and fast waves, and mode-conversion between the two, are self-consistently accounted for.

The values of $\Sigma_{\text{eff},j \rightarrow j'}$ and $\tilde{\sigma}_{\text{eff},j \rightarrow j'}(\chi)$ depend on k_{\parallel} and \mathbf{r} . They are implemented in GENRAY as lookup tables parameterized by k_{\parallel} , ψ , and θ_p (where ψ is the normalized radial coordinate and θ_p is the poloidal coordinate typically used in tokamaks). The filament statistics (and therefore the scattering probabilities) are made to vary such that relative

density fluctuations increase with outward distance from the separatrix. Due to the ballooning nature of SOL turbulence, fluctuations are smaller on the high field side. This is accounted for via the θ_p dependence of the scattering probabilities. For simplicity, f_p is assumed constant (though it can also be made to vary spatially). Details on the radial and poloidal tapering of scattering probabilities can be found in [appendix](#).

3. Application to Alactor C-Mod

A well-studied [11, 16, 29, 30] low- \bar{n}_e , fully non-inductive discharge (#1101104011) is modeled in GENRAY/CQL3D. Both HXR and MSE measurements are available, allowing for direct comparison to the simulated current density HXR count profiles. In modelling a quasi-steady-state time-slice at which $V_{\text{loop}} \approx 0$, it can be safely assumed that Ohmic contribution to the current profile is negligible.

Smooth electron density and temperature profiles are fit to Thompson scattering measurements. A kinetic EFIT profile is used (constrained by MSE measurements and produced in [11]). To model the SOL geometry, the two-point model is used to generate n, T profiles outside the separatrix [39]. It is assumed that the SOL e-folding width $\lambda_{\text{SOL}} = 7$ mm, and that $Z_{\text{eff}} = 1.5$ everywhere.

3.1. Scattering probabilities

The filament joint-PDF $p(n_b/n_0, a_b)$ is assumed to be a bivariate normal distribution. Relevant parameters include the average ($\langle \dots \rangle$), standard deviation (s), and skewness (Γ) for n_b/n_0 and a_b . (See [appendix](#) for a complete definition of these parameters, and how they vary radially and poloidally. Figures 12 and 13 summarize the spatial variations of the filament PDF).

For the purposes of illustrating how scattering probabilities vary in the SOL, it is assumed that $\langle n_0/n_b \rangle_{\text{grill}} = 3$, $\langle a_b \rangle = 0.5$ cm, $s_{a_b} = 0.2$ cm, and $\Gamma_{a_b} = 7$. (The parameter $\langle n_0/n_b \rangle_{\text{grill}}$ sets $\langle n_0/n_b \rangle$ at the LH antenna.) Figure 1 plot $\Sigma_{\text{eff}, i \rightarrow j}(\psi, \theta_p)$ for $N_{\parallel} = 1.6$ and $f_p = 0.2$ (though one can argue that so high a f_p is not strictly valid given the discussion in section 2.3). As expected, scattering is strongest in the far-SOL at the outer mid-plane, where $\Sigma_{\text{eff}, S \rightarrow F} \approx 40 \text{ m}^{-1}$. Conversely, scattering is weakest further into the core and closer to the inner mid-plane. Striations and local maxima in these plots, most notably for $\Sigma_{\text{eff}, S \rightarrow S}$ and $\Sigma_{\text{eff}, F \rightarrow F}$, are evidence of resonances akin to those found in Mie-scattering.

It should be noted that, while $S \rightarrow F$ and $F \rightarrow S$ are ‘opposite’ scattering events, their probabilities are not equal. Within the range of parameters tested, it is most common that $\Sigma_{\text{eff}, F \rightarrow S} > \Sigma_{\text{eff}, S \rightarrow F}$. In other words, there is preferential scattering from $S \rightarrow F$.

Asymmetric scatter (in angle space) is a full-wave effect, and is found to make a significant modification to the LH wave-spectrum. The physical explanation for asymmetric scatter is discussed in [30]. Figure 2 plots the effective asymmetric scatter metric $\alpha_{\text{eff}, i \rightarrow j}$, defined as:

$$\alpha_{\text{eff}, j \rightarrow j'} \equiv \int_0^{\pi} \langle \hat{\sigma}_{j \rightarrow j'}(\chi) \rangle d\chi - \frac{1}{2}. \quad (11)$$

An $\alpha_{\text{eff}, j \rightarrow j'} > 0$ (< 0) corresponds to scatter from mode j to j' preferentially in the $+\chi$ ($-\chi$) direction. Since LH waves are generally launched with $N_{\parallel} < 0$ in order to drive co-current, it can be shown that preferential $+\chi$ rotation equates to preferential scatter *away* from the plasma core. Conversely, $-\chi$ rotation leads to scattering *towards* the core. Figures 1 and 2 show the strongest asymmetry is from $S \rightarrow S$ scatter (in the sense that $\Sigma_{\text{eff}, S \rightarrow S}$ is rather large and $|\alpha_{\text{eff}, S \rightarrow F}|$ is robustly positive). Thus, there is a net scatter of power away from the core everywhere in the SOL. Although not shown here, this trend is insensitive to N_{\parallel} in the ranges expected in C-Mod.

3.2. Parametric scan of turbulence parameters

As a metric for simulation accuracy compared to experiment, we define the *normalized mean squared error* for an arbitrary simulated measurement X as

$$\bar{S}^2 = \frac{\|X_{\text{sim}} - X_{\text{exp}}\|}{\|X_{\text{simref}} - X_{\text{exp}}\|} \quad (12)$$

where ‘sim’ denotes the simulated values, ‘exp’ the experimental values, and ‘simref’ the simulated values in the reference (no turbulence) case. Further, we define $\bar{S}_{J_\phi}^2$ as replacing the array X in equation (12) with toroidal current density (J_ϕ) evaluated at the radial grid points modeled in CQL3D.

A parametric scan of parameters $\langle n_b/n_0 \rangle_{\text{grill}}$, $\langle a_b \rangle$, and f_p is conducted. Figure 3 plots contours of $\bar{S}_{J_\phi}^2$. It is evident that $\bar{S}_{J_\phi}^2$ decreases as turbulence intensity increases. Here, we define ‘turbulence intensity’ to mean the spatially averaged inverse scale length of density

$$\langle \langle L^{-1} \rangle \rangle \equiv \langle \langle |\nabla n|/n_0 \rangle \rangle \approx f_p \langle n_b/n_0 \rangle / \langle a_b \rangle \quad (13)$$

where $\langle \langle \dots \rangle \rangle$ denotes a spatial average. A minimum $\bar{S}_{J_\phi}^2 \approx 0.15$ is achieved for $\langle \langle L^{-1} \rangle \rangle \approx 30 \text{ m}^{-1}$, signifying a near seven-fold decrease in error. Interestingly, $\bar{S}_{J_\phi}^2$ remains near 0.15 for $\langle \langle L^{-1} \rangle \rangle \gtrsim 30 \text{ m}^{-1}$. This suggests that the impact of scattering on LHCD saturates for sufficiently high turbulence intensity, and that this condition is met in experiment.

This is further illustrated by focusing on two points in the turbulence parameter space. The point $[\langle n_b/n_0 \rangle_{\text{grill}}, \langle a_b \rangle, f_p] = [3, 0.5 \text{ cm}, 0.2]$ is termed ‘high’ turbulence, as it results in saturated state (see blue box in figure 3). The point $[\langle n_b/n_0 \rangle_{\text{grill}}, \langle a_b \rangle, f_p] = [1.5, 1 \text{ cm}, 0.2]$ is termed ‘low’ turbulence, as $\bar{S}_{J_\phi}^2 \approx 0.6$ and is therefore not fully saturated (see green box in figure 3). Figure 4 plots the corresponding current density and HXR profiles. The reference case predicts a largely hollow current profile with peaks at $\psi \approx 0.1$ and 0.8 . Correspondingly, the HXR profile is flat since this is a line-integrated diagnostic. These profiles are a poor match to the experiment. In contrast, the high turbulence case fully mitigates the off-axis peak in the current density profiles, and fills in the current ‘valley’ in the $\psi \approx 0.2 - 0.7$ region. (Note that small fluctuations in the simulated ‘high turb.’ current profile are a numerical artefact. They can be minimized by further increasing the number of rays simulated. In reality, fluctuations at this scale would be smoothed over by radial diffusion of fast electrons.) Consequently, the HXR profile is peaked in the middle channels

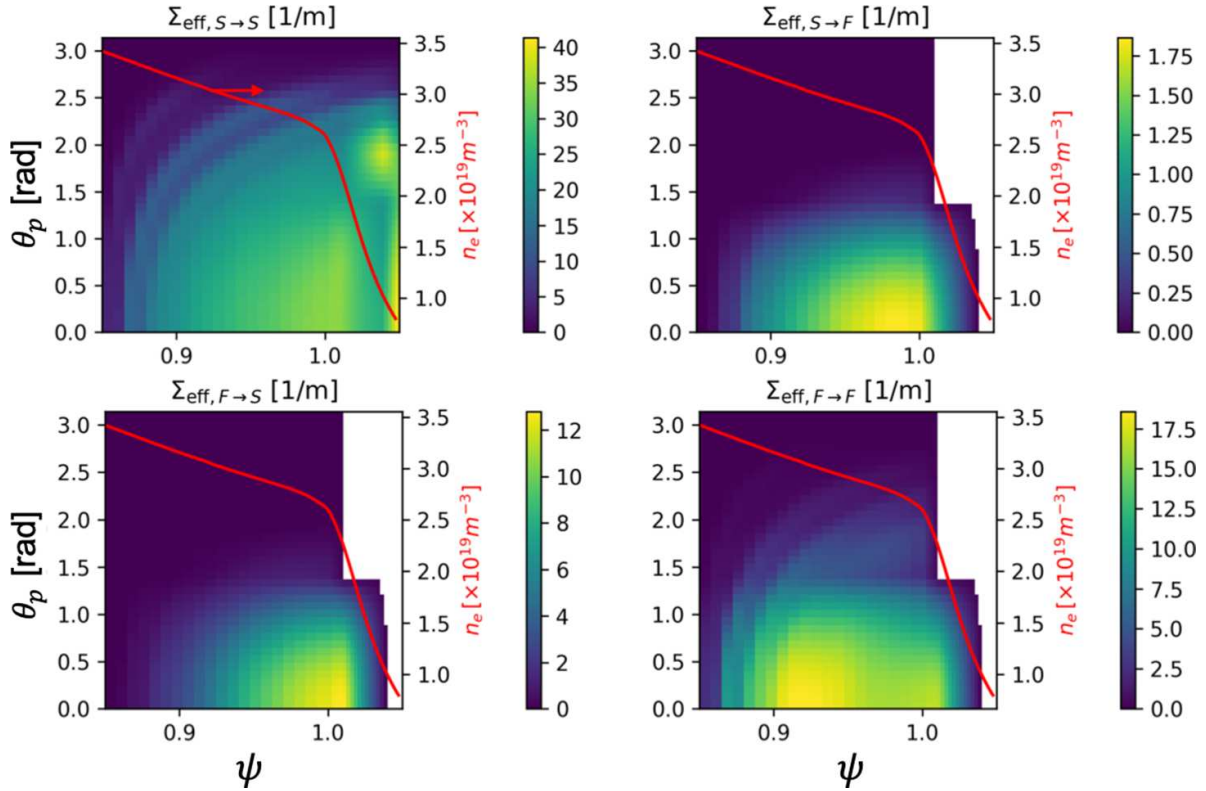


Figure 1. $\Sigma_{\text{eff},i \rightarrow j}(\psi, \theta_p, N_{||} = 1.6)$ plotted for $\langle n_0/n_b \rangle_{\text{grill}} = 3$, $\langle a_b \rangle = 0.5 \text{ cm}$, $s_{a_b} = 0.2 \text{ cm}$, $\Gamma_{a_b} = 7$, and $f_p = 0.2$. The white regions correspond to an evanescent FW. The red line indicates background density.

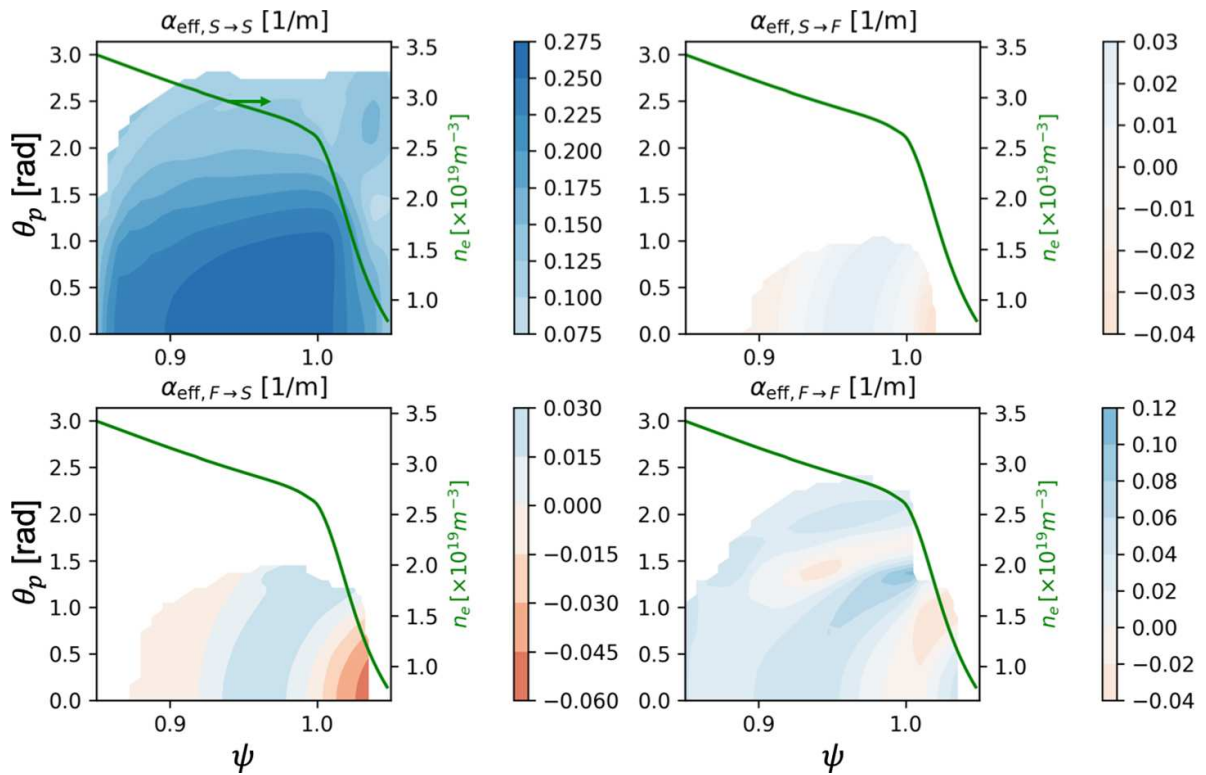


Figure 2. Asymmetric scattering metric $\alpha_{\text{eff},i \rightarrow j}(\psi, \theta_p, N_{||} = 1.6)$ plotted for same filament joint-PDF's as in figure 1. White regions correspond to $\Sigma_{\text{eff},i \rightarrow j} < 1 \text{ m}^{-1}$, where scattering is negligible. The green line indicates background density.

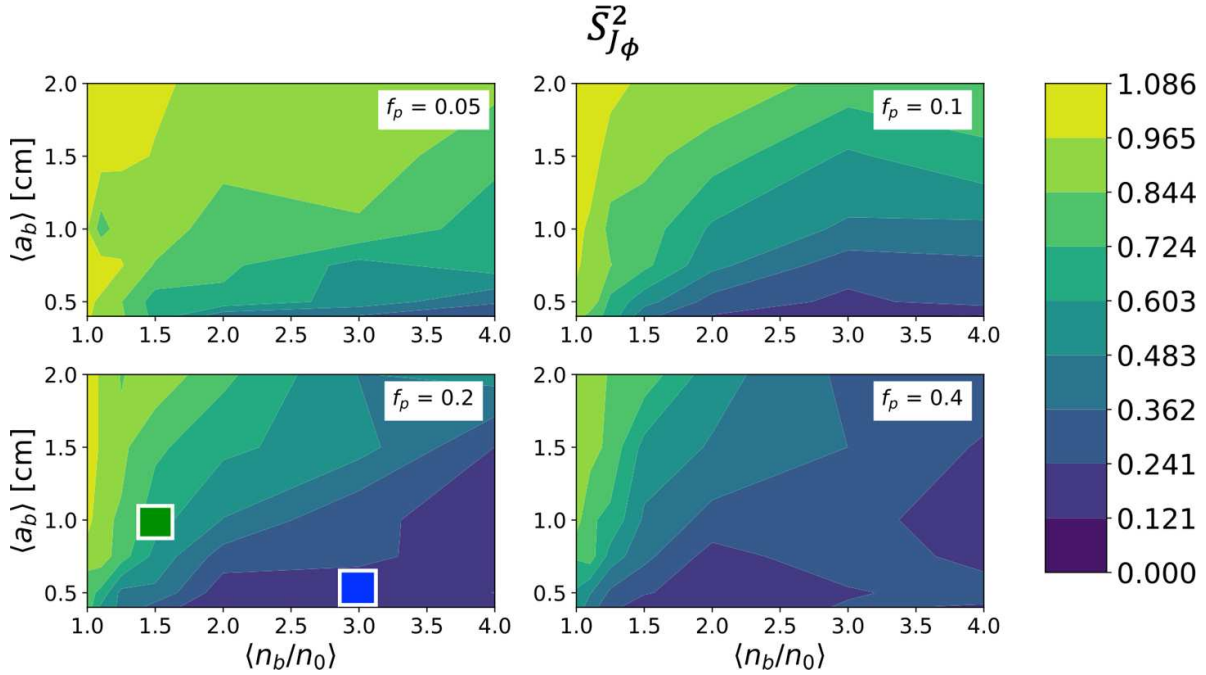


Figure 3. Parametric scan of turbulence parameters in GENRAY/CQL3D for discharge # 1101104011. Plotted are contours of $\bar{S}_{J\phi}^2$ (defined in equation (12) with X replaced by the toroidal current drive profile). Green box: low turbulence case. Blue box: high turbulence case.

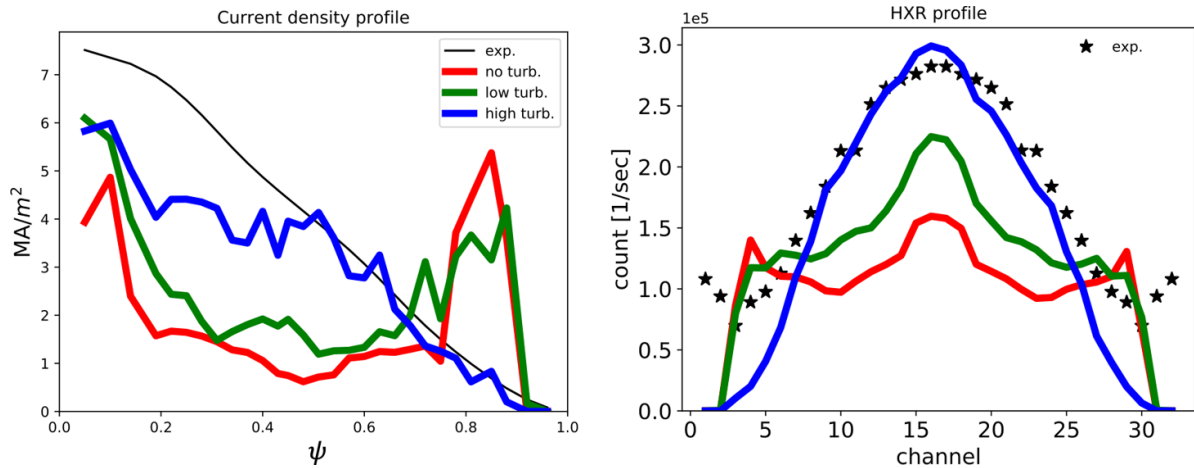


Figure 4. Current density (left) and HXR (right) profiles calculated in GENRAY/CQL3D for discharge # 1101104011. Low and high turbulence correspond to points in figure 3. Note: CQL3D top-down symmetrizes the plasma profile along the mid-plane, resulting in simulated HXR profiles roughly symmetric with respect to the middle channels (16 and 17). For proper comparison, the experimental HXR profile is also symmetrized.

and smoothly decays outwards. These profiles exhibit greatly improved agreement with experiment, although there remains a $\sim 20\%$ underestimation of current density on-axis. The low turbulence case is qualitatively a mix of the saturated and reference case. Off-axis peaks are somewhat mitigated, and near-axis current is also somewhat increased compared to the reference case.

3.3. Diffusion of ray-trajectories

The scattering-induced diffusion of rays can be observed in both real- and phase-space. Figure 5 plots ray-trajectories in the poloidal plane during the first pass. In the reference case,

ray damping in the core is negligible. In the high turbulence case, the initial ray bundle has greatly ‘fanned’ due to scattering. It should be emphasized that in figure 5 is only plotting ray-trajectories during *first-pass*, so what is shown is purely a scattering effect, and not due to ray-stochasticity following multiple reflections/passes. A fraction of rays scatter inwards, such that they strongly Landau damp in the hot near-axis region. This seeds a super-thermal electron tail near-axis, on which rays can further damp on subsequent passes. This explains the significant increase in near-axis current drive when scattering is included in the simulations.

Figure 6 plots ray-trajectories in phase-space for the reference and high turbulence case, showing only rays with

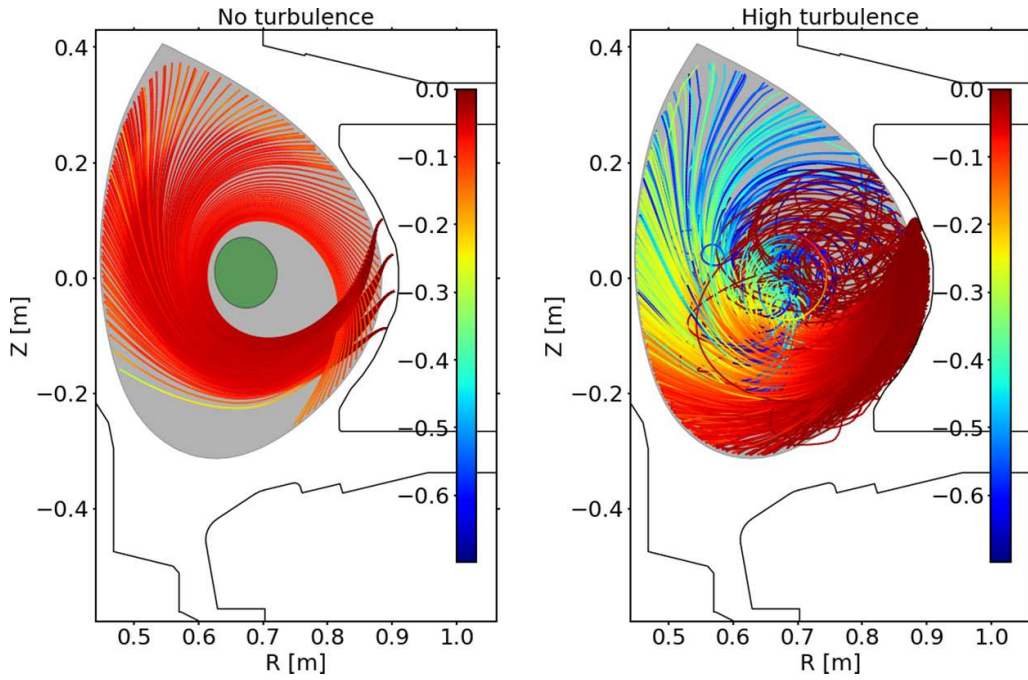


Figure 5. Ray-trajectories during first pass through the core. Plotting rays launched with $N_{||0} = 1.6 \pm 0.1$. Ray color denotes \log_{10} of normalized ray power. Green patch denotes region with $\psi \leq 0.2$.

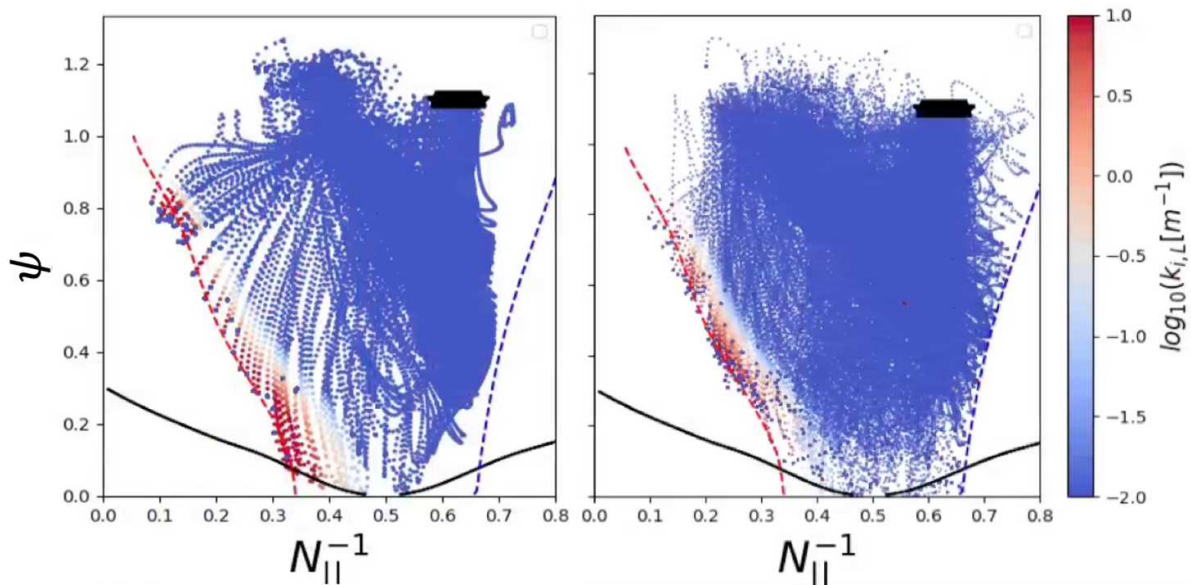


Figure 6. Ray-trajectories in phase-space for the reference (left) and high turbulence (right) cases. Plotting rays with $N_{||0} = 1.6 \pm 0.1$. The thick black bar denotes start of rays, and ray color denotes imaginary component of wave-vector due to Landau damping. Red dashed line: strong linear ELD condition as defined in equation (1). Blue dashed line: the Stix–Golant [40] accessibility condition. For completeness, we also plot the generalized accessibility condition [41, 42] in solid-black, though it is not a particularly relevant limit in C-Mod.

$N_{||,0} = 1.6 \pm 0.1$. These rays are confined between the strong ELD contour (equation (1)) in dashed-red, and the Stix–Golant [40] accessibility contour in dashed-blue. After multiple passes, they eventually damp near the ELD contour. Two observations are made about the reference case. (a) Even though a wide sample of rays in $N_{||0}$ space is plotted, the allowable phase-space is only partially and non-uniformly filled in. (b) There is a distinct bundle of rays that strongly Landau damps at $\psi \approx 0.8$. This causes the off-axis peak in the current density profile in figure 4.

Compare this to the high turbulence case, where phase-space is more uniformly filled in due to a strong diffusion of ray-trajectories caused by scattering. One particular result of this is the complete disappearance of the off-axis ray bundle.

3.4. High density partially inductive discharges

Two higher density discharges, with partially non-inductive current drive, are modeled in GENRAY/CQL3D.

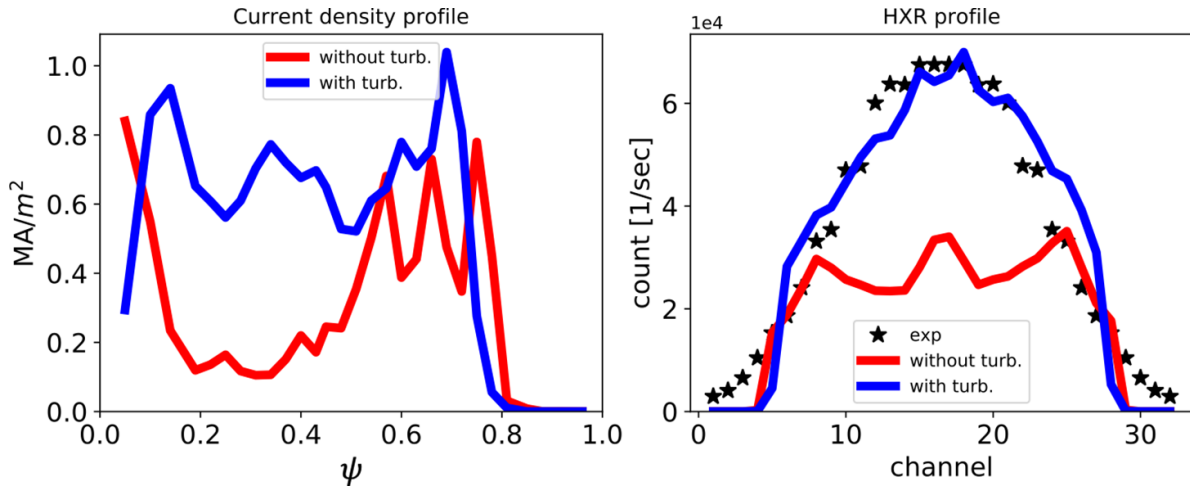


Figure 7. Current density (left) and HXR (right) profiles calculated in GENRAY/CQL3D for discharge #1140411016 for which $\bar{n}_e = 0.8 \times 10^{20} \text{ m}^{-3}$, $T_{e0} = 2.2 \text{ keV}$, and $[(n_b/n_0)_{\text{grill}}, (a_b), f_p] = [3, 0.5 \text{ cm}, 0.2]$.

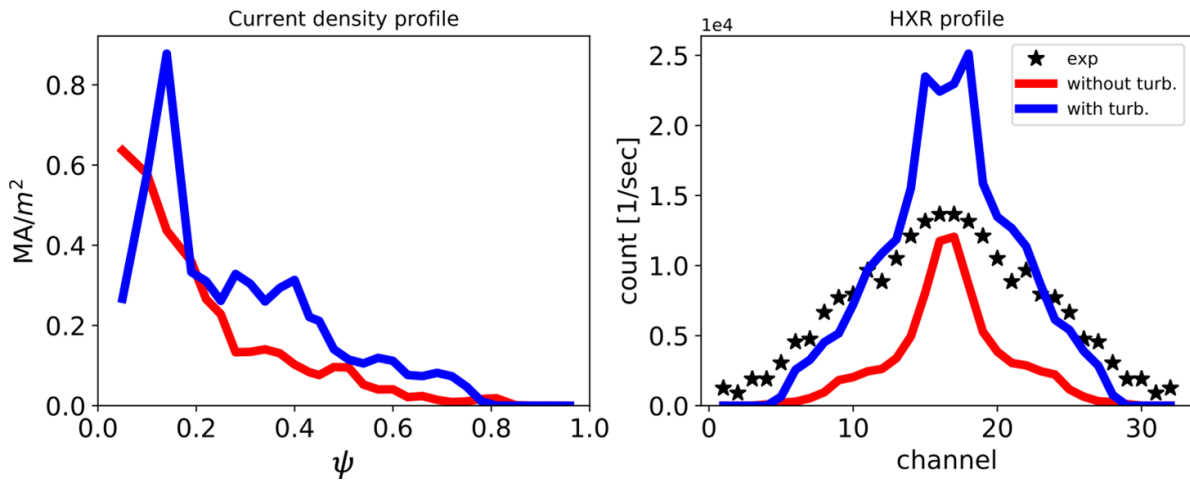


Figure 8. Current density (left) and HXR (right) profiles calculated in GENRAY/CQL3D for discharge #1140411015 for which $\bar{n}_e = 1.1 \times 10^{20} \text{ m}^{-3}$, $T_{e0} = 1.8 \text{ keV}$, and $[(n_b/n_0)_{\text{grill}}, (a_b), f_p] = [3, 0.5 \text{ cm}, 0.2]$.

In the first discharge (#1140411016), 460 kW of LH power launched at $N_{||0} = 1.9$ is coupled to an L-mode plasma with $\bar{n}_e = 0.8 \times 10^{20} \text{ m}^{-3}$ and $T_{e0} = 2.2 \text{ keV}$. During the LH phase, V_{loop} decreases from 1 V to 0.4 V. In the second discharge (#1140411015), 450 kW of LH power launched at $N_{||0} = 1.9$ is coupled to plasma with $\bar{n}_e = 1.1 \times 10^{20} \text{ m}^{-3}$ and $T_{e0} = 1.8 \text{ keV}$. Correspondingly, loop voltage drops from 0.95 V to 0.75 V. Note that this plasma is above the LHCD density limit [43], which explains the relatively small change in loop voltage. The DC electric field is neglected during CQL3D modeling of both discharges. There remain large uncertainties about the DC field radial profile, which can significantly modify the current profile. This can be accurately accounted for using time-dependent simulations as done by Poli *et al* [44].

Figures 7 and 8 plot the simulated current density and HXR profiles for the $\bar{n}_e = 0.8$ and $1.1 \times 10^{20} \text{ m}^{-3}$ discharges, respectively. The cases with turbulence use the same filament parameters as the high turbulence case identified in section 3.2. No attempt is made to compare to experimental

current densities. MSE measurements were not available for these discharges to reconstruct the current profile. Even if it were available, it is difficult to calculate the Ohmic and non-inductive contributions separately because the DC electric field profile is not known.

Notably, for the $\bar{n}_e = 0.8 \times 10^{20} \text{ m}^{-3}$ discharge, the current valley at $\psi \approx 0.3$ disappears when scattering is modelled. For both discharges, turbulence results in greater current drive near-axis ($\psi < 0.4$), ultimately leading to improved agreement with HXR profile measurements.

Similar to the low-density fully non-inductive case, a scan of filament parameters is conducted for the $\bar{n}_e = 0.8 \times 10^{20} \text{ m}^{-3}$ discharge in figure 9. Given that the experimental current drive profile cannot be isolated, we instead plot \bar{S}_{HXR}^2 , for which the array X in equation (12) is replaced with count rates from the 32-channel HXR diagnostic. It is evident that the saturation effect of SOL turbulence on LHCD is also present at high densities, in this case for $\langle\langle L^{-1} \rangle\rangle \gtrsim 15 \text{ m}^{-1}$. Thus, it is confirmed that the high turbulence parameters identified as being in the saturated regime for the low density

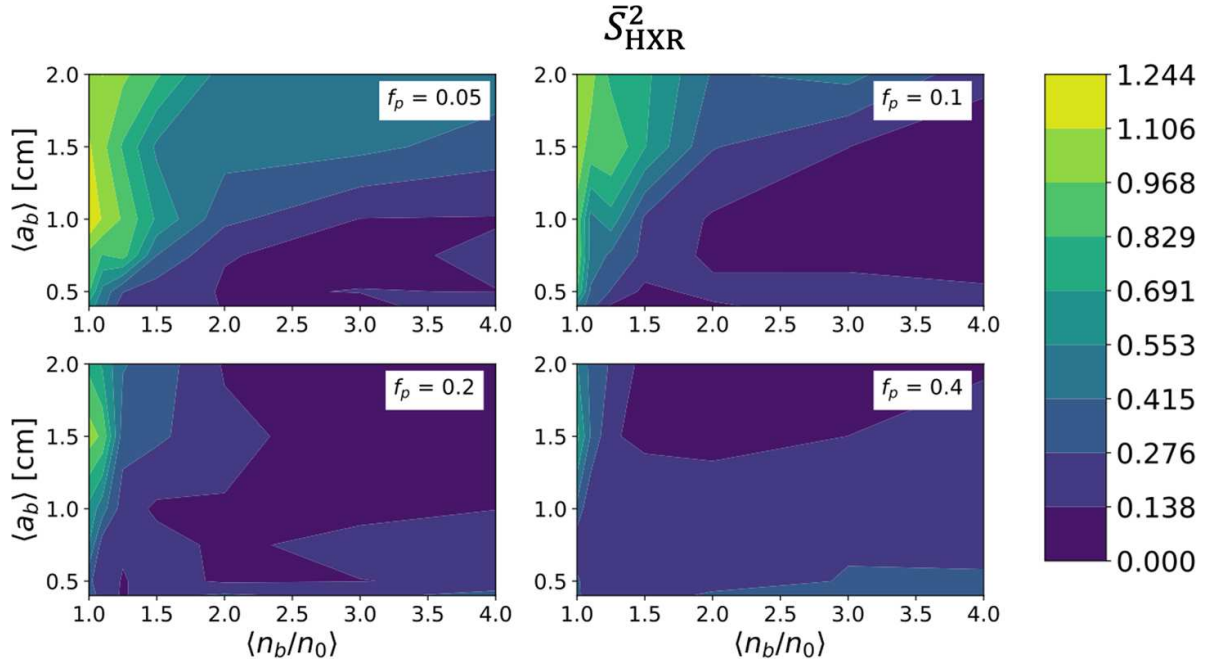


Figure 9. Parametric scan of turbulence parameters in GENRAY/CQL3D for discharge #1140411015. Plotted are contours of \bar{S}_{HXR}^2 (defined in equation (12) with X replaced by the HXR profile).

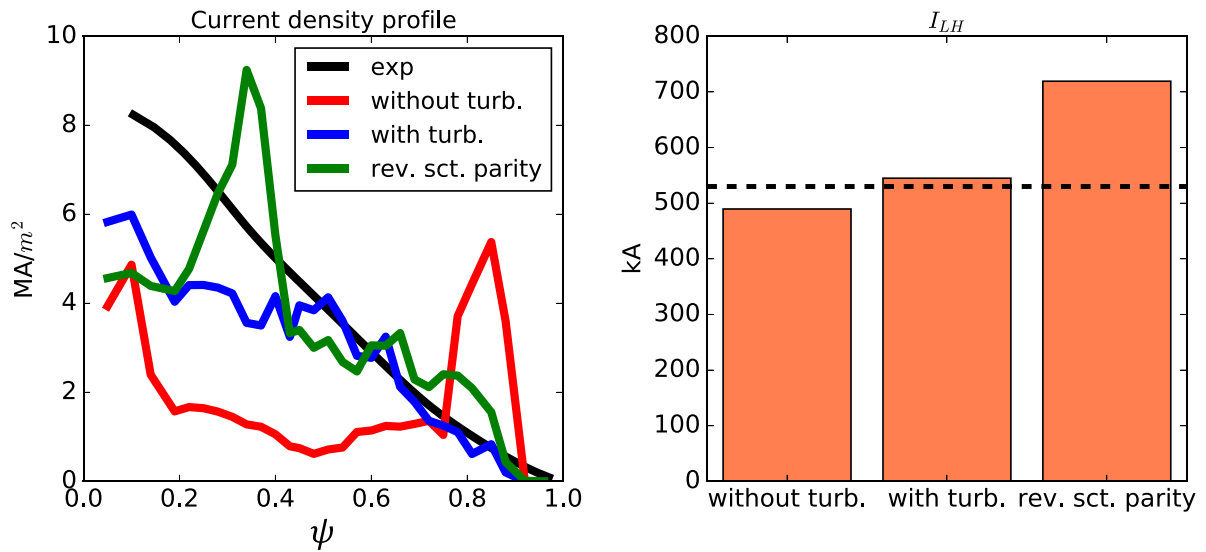


Figure 10. Current density profiles calculated in GENRAY/CQL3D for discharge #1101104011. Testing a reversed scattering parity. Horizontal dashed line denotes experimental value.

($\bar{n}_e = 0.52 \times 10^{20} \text{ m}^{-3}$) case, is also in the saturated regime for higher density discharges.

3.5. Impact of scattering asymmetry

As mentioned in section 3.1, the dominant asymmetric scattering effect is $S \rightarrow S$ scatter. On average, this leads to rays rotating away from the core. In turn, these rays propagate longer distances in the SOL, where parasitic collisional damping is non-negligible. One might then expect that less current is driven when asymmetric scatter is accounted for. A simple gedanken experiment is conducted to test this hypothesis.

Three cases are run: (a) the reference case, (b) a case with the usual scattering model, and (c) a case with the scattering model assuming reversed parity. Here, a reversal of parity means setting $\sigma_{\text{eff},j \rightarrow j'}(\chi) \rightarrow \sigma_{\text{eff},j \rightarrow j'}(-\chi)$, such that, on average, rays scatter *towards* the core.

First, this gedanken experiment is conducted for the low density fully non-inductive C-Mod discharge. Figure 10 plots resulting current density profiles. It is revealed that flipping the scattering parity does indeed affect the profile. In the reverse parity case, a large current density peak forms at $\psi \approx 0.2 - 0.4$. Relative to the normal scattering case, the reverse parity case results in $\sim 30\%$ greater current drive. This trend is

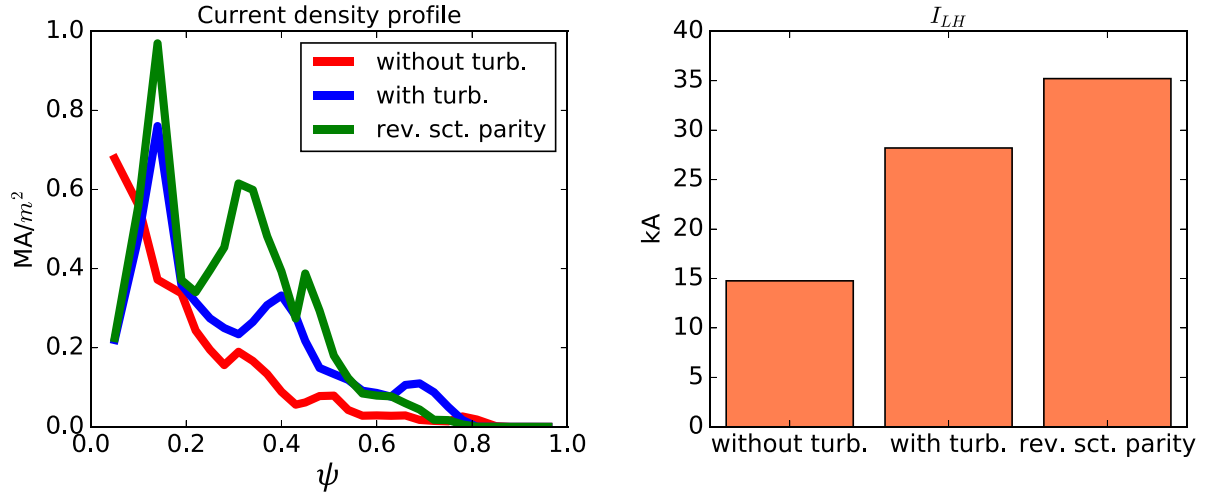


Figure 11. Current density profiles calculated in GENRAY/CQL3D for discharge #1140411015. Testing a reversed scattering parity. Simulated current profile not compared to experimental measurements because the Ohmic contribution is neglected in the model.

as expected. This experiment is repeated with the $\bar{n}_e = 1.1 \times 10^{20} \text{ m}^{-3}$ discharge, with figure 11 plotting current density profiles. A reversed scattering parity results in significantly greater near-axis current deposition, and $\sim 25\%$ greater total current drive compared to the normal scattering case.

Contrary to the hypothesis, the normal parity case results in greater current than in the reference case. An explanation for this can be found in examining figure 5. While there is a net rotation of rays away from the core, there is still a large fraction of rays rotated towards the core such that they damp on-axis during first pass. In contrast, virtually no power damps on-axis during first pass in the reference case. Thus, this effect is enough to counteract the net outward scatter.

4. Summary and discussion

A multiscale model has been developed for LH wave propagation in a magnetized plasma with filamentary turbulence. Wave propagation is computed using ray-tracing. Relatively expensive full-wave calculations are reserved only for wave-filament interactions, which then act as stochastic kicks to the ray-trajectories. The scattering probabilities are spatially dependent, which allows the prescription of a radially and poloidally tapered SOL turbulence profile in a tokamak geometry. In addition, both like- and unlike-mode scattering is modelled.

This multiscale scattering model is applied to C-Mod discharges, where the impact of scattering on LHCD is shown to saturate at sufficiently high levels of turbulence intensity. In the saturated phase, ray-trajectories are significantly diffused in phase-space. In turn, LHCD predictions are insensitive to the assumed turbulence parameters. At low density ($\bar{n}_e \approx 0.52 \times 10^{20} \text{ m}^{-3}$), the saturated case results in excellent agreement with experimental MSE and HXR measurements. Here, a turbulence intensity of $\langle\langle L^{-1} \rangle\rangle \gtrsim 30 \text{ m}^{-1}$ resulted in saturation with $\bar{S}_{\text{HXR}}^2 < 0.15$, signifying a near seven-fold decrease in error for the current profile (compared to the simulation

with no scattering). This saturation is also present in the high density case above the LHCD density limit. Here, saturation at $\langle\langle L^{-1} \rangle\rangle \gtrsim 15 \text{ m}^{-1}$ results in significantly improved match to experiment ($\bar{S}_{\text{HXR}}^2 < 0.1$). This suggests that, experimentally, the impact of wave-filament scatter is saturated in C-Mod L-mode discharges for all background densities. In future work, it will be worthwhile to study how the threshold $\langle\langle L^{-1} \rangle\rangle$ depends on plasma and LH launch parameters.

While this modeling suggests that C-Mod LH launch is in this saturation regime, it is unclear whether this is corroborated by edge turbulence measurements. Analysis of Langmuir probe measurements in the SOL of C-Mod measure $\langle n_b/n_0 \rangle \approx 2.1$ [45]. Similarly, GPI measurements indicate $\langle a_b \rangle \approx 1 \text{ cm}$ [46] and $f_p \sim 0.05$ [47]. However, these burst statistic analyses require setting an arbitrary threshold above r.m.s. values for identifying a filament. This threshold affects the computed $\langle n_b/n_0 \rangle$, $\langle a_b \rangle$, and greatly affects f_p . Given the large experimental uncertainties in measuring these parameters, no attempt is made here in prescribing the likeliest filament PDF or packing fraction. Rather, it is argued that SOL measurements in C-Mod do not rule out the possibility of a saturated regime for LH wave scattering.

The impact of asymmetric scattering was tested by reversing the scattering parity. The reversed parity leads to increased scatter of LH power into the core. As expected, this results in greater current drive and HXR count compared to simulations with the correct scattering parity. It is important to note, however, that scatter with correct parity, which results in net outward scatter, still leads to greater current drive than the case with no scattering. This is attributed to the non-zero fraction of LH power that scatters inwards and Landau damps near-axis on first pass.

In regards to the three C-Mod discharges modelled in this work, it is interesting to note that the simulated HXR count, for both the reference and high turbulence cases, agree within an order of magnitude with the experimental values. This is in stark contrast to previous analysis, in which standard

ray-tracing/Fokker–Planck simulations could not replicate the anomalous drop in total current driven and HXR count for $\bar{n}_e \gtrsim 10^{20} \text{ m}^{-3}$ [11, 43]. However, later simulations including a more realistic collisional SOL could successfully do so [39]. This present work uses this improved SOL model. Overall, this suggests that proper modeling of SOL collisional losses is needed to accurately calculate *total* current and HXR count, while proper modeling of scattering is needed to accurately calculate the *radial profile* of current and HXR count.

The above considerations should *not* suggest that PDI is unimportant. Scattering and PDI are not mutually exclusive mechanisms, and the interplay between them remain an interesting challenge for LHCD modelling. PDI is likely a significant factor in the SOL at high densities ($\bar{n}_e \gtrsim 1 \times 10^{20} \text{ m}^{-3}$) due to increasing homogeneous and convective growth rates [22, 48]. Consider the low density case in figure 4, where the simulated HXR profile with scattering effects is in excellent agreement with experimental measurements. The same cannot be said for the high density case in figure 8, in which simulations over-predict HXR count in the middle channels (#11–23). Additional physics, possibly spectral broadening via PDI, may explain this discrepancy. In fact, there is evidence of large ion cyclotron side-bands and significant pump depletion during LH launch in high density C-Mod discharges, which strongly suggests parametric decay to ion cyclotron quasi-modes [22]. This is another possible explanation for the LHCD density limit in C-Mod.

Lastly, it should be emphasized that these multiscale simulations allow, for the first time, the coupling of wave-filament scattering physics, beyond ray-tracing, to the down-stream physics of core damping and current drive. This is of practical importance for the following reason. It has been shown, through the use of this multiscale model, that accurate simulation of LHCD requires accounting for wave-filament scatter from sufficiently intense SOL turbulence. This corresponds to a situation in which ray-tracing is invalid, and so higher-order scattering effects must be taken into account. This is evidenced by the relatively poor performance of the filament refraction model which employed ray-tracing alone [29]. While global full-wave simulations are computationally intensive, this multiscale approach applies full-wave calculations only locally where it is needed (at the wave–filament interaction). In this way, fast parametric scans and intershot analysis is made possible on modest, university-scale computing clusters. For example, consider figure 3. This parametric scan consisted of 196 simulations and required ~ 3500 total CPU-hours on the Engaging cluster. (Equivalently, ~ 17.5 CPU-hours were required per simulation.)

Acknowledgments

This work was supported by US DoE under Contract Numbers: DE-SC0018090 supporting the RF-SciDAC 4 project, DE-SC0014264 supporting PSFC MFE projects, and DE-FC02-04ER54698 supporting DIII-D projects. The GENRAY/QQL3D simulations presented in this paper were

performed on the MIT-PSFC partition of the Engaging cluster at the MGHPCC facility (www.mghpcc.org) which was funded by DoE Grant Number DE-FG02-91-ER54109.

Conflict of interest

The authors report no conflict of interest.

Appendix. Radially and poloidally tapered turbulence

GENRAY uses (ψ, θ_p) -coordinates in the poloidal plane, where $\psi \equiv \sqrt{\Psi_\phi / \Psi_{\phi,a}}$ is the normalized radial coordinate (and Ψ_ϕ is toroidal magnetic flux). The evaluation of coordinate ψ is approximately extended outside the separatrix. It is approximated that $n(\mathbf{r}) \approx n(\psi, \theta_p)$. Given the relatively slow spatial variation of B , it is acceptable for our purposes of calculating scattering probabilities in the SOL to assume

$$B \approx B_\phi \approx \frac{B_0}{1 + \frac{a}{R_0} \cos(\theta_p)} \quad (\text{A.1})$$

where B_ϕ is the toroidal magnetic field and a, R_0 are the minor, major plasma radius.

In assuming that the turbulence parameters vary radially and poloidally (i.e. $p(n_b/n_0(\mathbf{r}), a_b(\mathbf{r})) = p(n_b/n_0, a_b; \psi, \theta_p)$), one can parametrize the scattering probabilities as $\hat{\sigma}_{\text{eff},j \rightarrow j'}(\chi; \psi, \theta_p, k_{\parallel})$ and $\Sigma_{\text{eff},j \rightarrow j'}(\chi; \psi, \theta_p, k_{\parallel})$. These form the lookup tables in GENRAY.

As in [30], it is assumed that the filament joint-PDF is a bivariate skewed Gaussian [49], now with radial and poloidal dependence. Its analytic form is written as a function of the 2D column vector $\zeta = [n_b/n_0; a_b]$, while parametrization depending on radial and poloidal coordinates is made explicit.

$$p(\zeta; \psi, \theta_p) = 2\phi_2(\zeta - Q(\psi, \theta_p)\Omega(\psi, \theta_p)) \times \Phi(\Gamma^T(\psi, \theta_p)[\zeta - Q(\psi, \theta_p)]) \quad (\text{A.2a})$$

$$\Omega(\psi, \theta_p) = \begin{bmatrix} s_{n_b/n_0}^2(\psi, \theta_p) & \eta s_{n_b/n_0}(\psi, \theta_p) s_{a_b} \\ \eta s_{n_b/n_0}(\psi, \theta_p) s_{a_b} & s_{a_b}^2 \end{bmatrix} \quad (\text{A.2b})$$

$$Q(\psi, \theta_p) = \langle \zeta \rangle(\psi, \theta_p) - \sqrt{\frac{2}{\pi}} \delta(\psi, \theta_p) \quad (\text{A.2c})$$

$$\delta(\psi, \theta_p) = \frac{1}{\sqrt{1 + \Gamma^T \Omega(\psi, \theta_p) \Gamma}} \Omega(\psi, \theta_p) \Gamma \quad (\text{A.2d})$$

$$\Gamma(\psi, \theta_p) = \begin{bmatrix} \Gamma_{n_b/n_0}(\psi, \theta_p) \\ \Gamma_{a_b} \end{bmatrix} \quad (\text{A.2e})$$

where $\phi_2(\zeta, \Omega)$ is a 2D Gaussian PDF with zero mean and correlation matrix Ω , $\Phi(x)$ is the 1D Gaussian CDF for scalar input x , Γ is now a 2D column vector of skewness factors, and $\langle \zeta \rangle \equiv [\langle n_b/n_0 \rangle; \langle a_b \rangle]$ is the 2D column vector of mean n_b/n_0 and a_b . Similarly, $s \equiv [s_{n_b/n_0}; s_{a_b}]$ are standard deviations, and

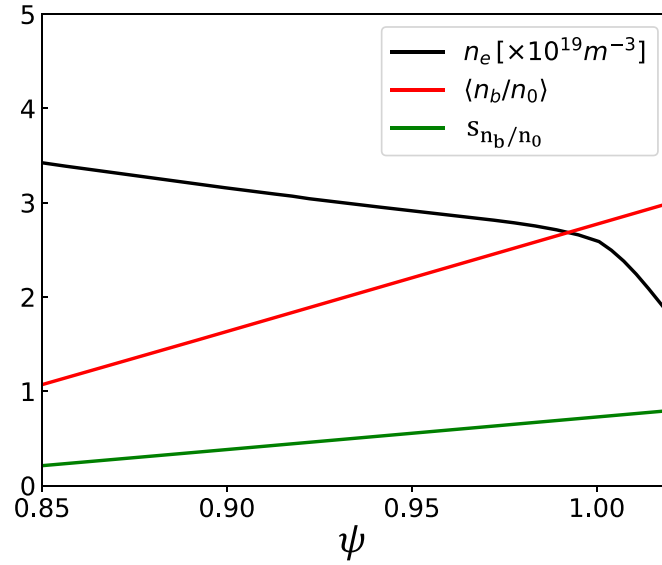


Figure 12. Background density and modeled turbulence profile at the outer mid-plane in a C-Mod discharge. The only user-specified parameter is $\langle n_0/n_b \rangle_{\text{grill}} = 3$. The $\langle n_b/n_0 \rangle$ and s_{n_b/n_0} profiles are prescribed according to equations (A.3)–(A.5).

η is the scalar correlation coefficient. It is therefore possible to parameterize $p(\zeta)$ as a function of $\langle \zeta \rangle$, Γ , s , η , ψ , and θ_p . In contrast to [30], the filament relative density mean ($\langle n_b/n_0 \rangle$), standard deviation (s_{n_b/n_0}), and skewness (Γ_{n_b/n_0}) are allowed to vary with ψ and θ_p . For simplicity, the filament width statistics ($\langle a_b \rangle$, s_{a_b} , and Γ_{a_b}) are kept homogeneous. Further, it is assumed that $s_{a_b} = 0.2$ cm and $\Gamma_{a_b} = 7$. The correlation coefficient $\eta = 0.9$, signifying strong positive correlation between n_b/n_0 and a_b [50].

The radial profile for fluctuations should smoothly increase from zero inside the separatrix to the user-specified $\langle n_b/n_0 \rangle_{\text{grill}}$ at the LH grill. The following analytic forms are assumed for $\langle n_b/n_0 \rangle$, s_{n_b/n_0} and Γ_{n_b/n_0} :

$$\langle n_b/n_0 \rangle = [\langle n_b/n_0 \rangle_{\text{min}} + (\langle n_b/n_0 \rangle_{\text{grill}} - \langle n_b/n_0 \rangle_{\text{min}}) \bar{\psi}^{g(\theta_p)}] + 1 \quad (\text{A.3a})$$

$$s_{n_b/n_0} = [s_{n_b/n_0, \text{min}} + (s_{n_b/n_0, \text{grill}} - s_{n_b/n_0, \text{min}}) \bar{\psi}^{g(\theta_p)}] \quad (\text{A.3b})$$

$$\Gamma_{n_b/n_0} = [\Gamma_{n_b/n_0, \text{min}} + (\Gamma_{n_b/n_0, \text{grill}} - \Gamma_{n_b/n_0, \text{min}}) \bar{\psi}^{g(\theta_p)}] \quad (\text{A.3c})$$

where

$$\bar{\psi}(\psi) = \begin{cases} 0 & \psi < \psi_{\text{min}} \\ (\psi - \psi_{\text{min}})/(\psi_{\text{grill}} - \psi_{\text{min}}) & \psi_{\text{min}} < \psi < \psi_{\text{grill}} \\ 1 & \psi > \psi_{\text{grill}} \end{cases} \quad (\text{A.4})$$

and ψ_{grill} is the radial location of the LH launcher (a.k.a. grill). In this study, the minimum radial location of non-zero turbulence (ψ_{min}) is set to 0.85. It is assumed that $\langle n_b/n_0 \rangle_{\text{min}} = 1$, $s_{n_b/n_0, \text{min}} = 0.1$, $\Gamma_{n_b/n_0, \text{min}} = 0.01$, and $\Gamma_{n_b/n_0, \text{max}} = 7$. The following linear relation is used to prescribe $s_{n_b/n_0, \text{grill}}$:

$$s_{n_b/n_0, \text{grill}} = c_1 \left\langle \frac{n_b}{n_0} \right\rangle_{\text{grill}} + c_2 \quad (\text{A.5})$$

where c_1 and c_2 are set such that $s_{n_b/n_0, \text{grill}} = 1.1$ for $\langle n_b/n_0 \rangle_{\text{grill}} = 4$ and $s_{n_b/n_0, \text{grill}} = 0.22$ for $\langle n_b/n_0 \rangle_{\text{grill}} = 1.1$.

Lastly, the function $g(\theta_p)$ introduces a poloidal variation and is prescribed to be

$$g(\theta_p) = 0.1 + 0.9 \cos^2(\theta_p/2). \quad (\text{A.6})$$

This accounts for experimental measurements that density fluctuations on the HFS are greatly suppressed [51, 52].

Figure 12 plots background density and example turbulence profiles at the outer mid-plane for the non-inductive C-Mod discharge. In this case, the LH grill position corresponds to $\psi_{\text{grill}} \approx 1.02$. The free-parameter $\langle n_0/n_b \rangle_{\text{grill}} = 3$ prescribes mean relative density of filaments at the LH grill. The mean relative density of filaments monotonically decrease to unity at $\psi = 0.85$, meaning they are indistinguishable from the background, thereby smoothly transitioning into a quiescent core plasma.

Figure 13 shows an example of how the joint-PDF at $\psi = 1.02$ (in the SOL) is tapered poloidally such that filaments are, on average, less dense on the high-field side.

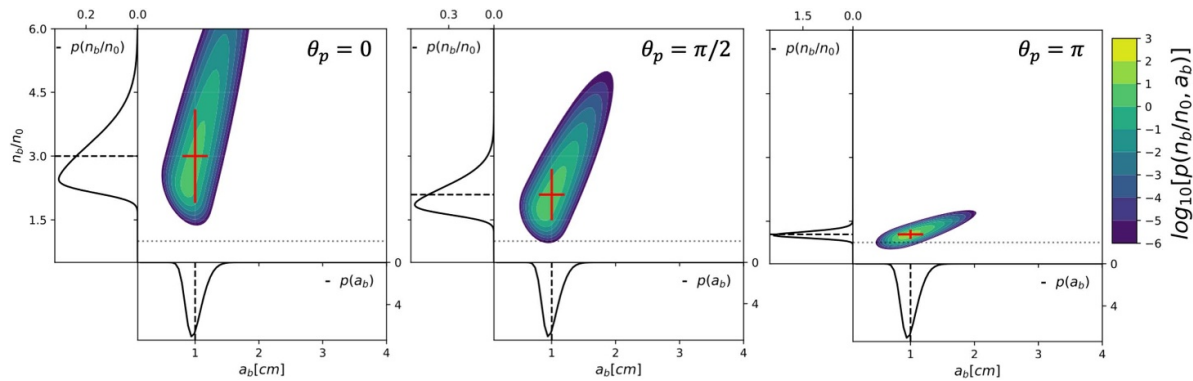


Figure 13. Joint-PDF of filament parameters for $\psi = 1.02$. The only user-specified parameters are $\langle n_0/n_b \rangle_{\text{grill}} = 3$ and $\langle a_b \rangle = 1$ cm. Red cross-hairs denote ± 1 standard deviation in n_b/n_0 and a_b .

ORCID iD

Bodhi Biswas  <https://orcid.org/0000-0001-7993-3732>

References

- [1] Fisch N.J. 1987 Theory of current drive in plasmas *Rev. Mod. Phys.* **59** 175–234
- [2] Ide S., Naito O., Oikawa T., Fujita T., Kondoh T., Seki M. and Ushigusa K. (JT-60 Team) 2000 LHCD current profile control experiments towards steady state improved confinement on JT-60U *Nucl. Fusion* **40** 445–51
- [3] Peysson Y. and Team T.S. 2001 High power lower hybrid current drive experiments in the Tore Supra tokamak *Nucl. Fusion* **41** 1703–13
- [4] Litaudon X. et al (Contributors to the EFDA-JET Workprogramme) 2002 Towards fully non-inductive current drive operation in JET *Plasma Phys. Control. Fusion* **44** 1057–86
- [5] Pericoli-Ridolfini V. et al 1999 High plasma density lower-hybrid current drive in the FTU Tokamak *Phys. Rev. Lett.* **82** 93–96
- [6] Shiraiwa S. et al The Alcator C-Mod team 2011 Design and initial experiment results of a novel LH launcher on Alcator C-Mod *Nucl. Fusion* **51** 103024
- [7] La Haye R.J. 2006 Neoclassical tearing modes and their control *Phys. Plasmas* **13** 055501
- [8] Reiman A.H. and Fisch N.J. 2018 Suppression of tearing modes by radio frequency current condensation *Phys. Rev. Lett.* **121** 225001
- [9] Bonoli P. 1984 Linear theory of lower hybrid heating *IEEE Trans. Plasma Sci.* **12** 95–107
- [10] Bonoli P.T. and Ott E. 1982 Toroidal and scattering effects on lower-hybrid wave propagation *Phys. Fluids* **25** 359
- [11] Mumgaard R.T. 2015 Lower hybrid current drive on Alcator C-Mod: measurements with an upgraded MSE diagnostic and comparisons to simulation *PhD Thesis MIT*
- [12] Peysson Y. (The TORE SUPRA Team) 2000 Progress towards high-power lower hybrid current drive in TORE SUPRA *Plasma Phys. Control. Fusion* **42** B87
- [13] Garofalo A. et al 2017 Development of high poloidal beta, steady-state scenario with ITER-like tungsten divertor on EAST *Nucl. Fusion* **57** 076037
- [14] Peysson Y. et al (HL-2A Team) 2020 Lower hybrid current drive in high aspect ratio tokamaks *J. Fusion Energy* **39** 270–91
- [15] Peysson Y. et al 2016 Advances in modeling of lower hybrid current drive *Plasma Phys. Control. Fusion* **58** 044008
- [16] Baek S. et al 2021 A model investigation of the impact of lower hybrid wave scattering angle on current drive profile in EAST and Alcator C-Mod *Nucl. Fusion* **61** 106034
- [17] Porkolab M. 1974 Theory of parametric instability near the lower-hybrid frequency *Phys. Fluids* **17** 1432
- [18] Cesario R., Cardinali A., Castaldo C., Paoletti F. and Mazon D. 2004 Modeling of a lower-hybrid current drive by including spectral broadening induced by parametric instability in tokamak plasmas *Phys. Rev. Lett.* **92** 175002
- [19] Madi M., Peysson Y., Decker J. and Kabalan K.Y. 2015 Propagation of the lower hybrid wave in a density fluctuating scrape-off layer (SOL) *Plasma Phys. Control. Fusion* **57** 125001
- [20] Cesario R. et al 2014 Spectral broadening of parametric instability in lower hybrid current drive at a high density *Nucl. Fusion* **54** 043002
- [21] Cesario R. et al 2010 Current drive at plasma densities required for thermonuclear reactors *Nat Commun* **1** 55
- [22] Baek S., Parker R., Bonoli P., Shiraiwa S., Wallace G., LaBombard B., Faust I., Porkolab M. and Whyte D. 2015 High density LHRF experiments in Alcator C-Mod and implications for reactor scale devices *Nucl. Fusion* **55** 043009
- [23] Bellan P.M. and Wong K.L. 1978 Effect of density fluctuations on lower hybrid resonance cone propagation *Phys. Fluids* **21** 592–9
- [24] Peysson Y., Decker J., Morini L. and Coda S. 2011 RF current drive and plasma fluctuations *Plasma Phys. Control. Fusion* **53** 124028
- [25] Andrews P.L. and Perkins F.W. 1983 Scattering of lower-hybrid waves by drift-wave density fluctuations: solutions of the radiative transfer equation *Phys. Fluids* **26** 2537–45
- [26] Bertelli N. et al 2013 The effects of the scattering by edge plasma density fluctuations on lower hybrid wave propagation *Plasma Phys. Control. Fusion* **55** 074003
- [27] Zweben S.J. et al 2002 Edge turbulence imaging in the Alcator C-Mod tokamak *Phys. Plasmas* **9** 1981–9
- [28] Graves J.P., Horacek J., Pitts R.A. and Hopcraft K.I. 2005 Self-similar density turbulence in the TCv tokamak scrape-off layer *Plasma Phys. Control. Fusion* **47** 1–9
- [29] Biswas B., Gyou Baek S., Bonoli P., Shiraiwa S., Wallace G. and White A. 2020 Study of turbulence-induced refraction of lower hybrid waves using synthetic scrape-off layer filaments *Plasma Phys. Control. Fusion* **62** 115006
- [30] Biswas B., Shiraiwa S., Baek S.-G., Bonoli P., Ram A. and White A.E. 2021 A hybrid full-wave Markov chain approach to calculating radio-frequency wave scattering from scrape-off layer filaments *J. Plasma Phys.* **87** 35

- [31] Frank S.J., Lee J.P., Wright J.C., Hutchinson I.H. and Bonoli P.T. 2022 Verifying raytracing/Fokker-Planck lower-hybrid current drive predictions with self-consistent full-wave/Fokker-Planck simulations (arXiv:2207.09011)
- [32] Ram A.K. and Hizanidis K. 2016 Scattering of radio frequency waves by cylindrical density filaments in tokamak plasmas *Phys. Plasmas* **23** 022504
- [33] Zhang W., Tierens W., Bobkov V., Cathey A., Cziegler I., Griener M., Hoelzl M., Kardaun O. and Bobkov V. 2021 Interaction between filaments and ICRF in the plasma edge *Nucl. Mater. Energy* **26** 100941
- [34] Myra J.R. and D'Ippolito D.A. 2010 Scattering of radio frequency waves by blob-filaments *Phys. Plasmas* **17** 102510
- [35] Tierens W., Bilato R., Bertelli N., Shiraiwa S., Myra J. and Colas L. 2022 On the origin of high harmonic fast wave edge losses in NSTX *Nucl. Fusion* **62** 096011
- [36] Mishchenko M.I. 2014 *Electromagnetic Scattering by Particles and Particle Groups: An Introduction* (Cambridge: Cambridge University Press)
- [37] Smirnov A. and Harvey R. 2001 The GENRAY ray tracing code *Technical Report* CompX
- [38] Harvey R.W. and McCoy M.G. 2005 The CQL3D Fokker-Planck Code (reconstituted in editable form from General Atomics Report GA-A20978, 1992) *Technical Report* (available at: <https://aip.scitation.org/doi/abs/10.1063/1.4936481>)
- [39] Shiraiwa S. *et al* 2015 Impact of SOL plasma profiles on lower hybrid current drive: experimental evidence, mitigation and modeling approaches *Radio Frequency Power in Plasmas: Proc. 21st Topical Conf., (California, USA)* p 030016
- [40] Stix T.H. 1992 *Waves in Plasmas* (Springer Science & Business Media)
- [41] Takahashi H. 1994 The generalized accessibility and spectral gap of lower hybrid waves in tokamaks *Phys. Plasmas* **1** 2254–76
- [42] Paoletti F., Ignat D.W., Kesner J., Bernabei S., Kaita R., Leblanc B., Levinton F.M. and Luckhardt S.C. 1994 Lower hybrid current drive accessibility study with reconstructed magnetic equilibria in PBX-M *Nucl. Fusion* **34** 771–6
- [43] Wallace G.M. *et al* 2011 Lower hybrid current drive at high density in Alcator C-Mod *Nucl. Fusion* **51** 083032
- [44] Poli F.M. *et al* 2016 Experimental and modeling uncertainties in the validation of lower hybrid current drive *Plasma Phys. Control. Fusion* **58** 095001
- [45] Kube R., Theodorsen A., Garcia O.E., Labombard B. and Terry J.L. 2016 Fluctuation statistics in the scrape-off layer of Alcator C-Mod *Plasma Phys. Control. Fusion* **58** 054001
- [46] Kube R., Garcia O., LaBombard B., Terry J. and Zweben S. 2013 Blob sizes and velocities in the Alcator C-Mod scrape-off layer *J. Nucl. Mater.* **438** S505–8
- [47] Zweben S.J. *et al* 2011 Estimate of convective radial transport due to SOL turbulence as measured by GPI in Alcator C-Mod *J. Nucl. Mater.* **415** S463–6
- [48] Baek S.G. *et al* 2014 Characterization of the onset of ion cyclotron parametric decay instability of lower hybrid waves in a diverted tokamak *Phys. Plasmas* **21** 061511
- [49] Azzalini A. and Capitanio A. 1999 Statistical applications of the multivariate skew normal distribution *J. R. Stat. Soc. B* **61** 579–602
- [50] Decristoforo G., Militello F., Nicholas T., Omotani J., Marsden C., Walkden N. and Garcia O.E. 2020 Blob interactions in 2D scrape-off layer simulations *Phys. Plasmas* **27** 122301
- [51] Terry J.L. *et al* 2003 Observations of the turbulence in the scrape-off-layer of Alcator C-Mod and comparisons with simulation *Phys. Plasmas* **10** 1739–47
- [52] Smick N., Labombard B. and Pitcher C.S. 2005 Plasma profiles and flows in the high-field side scrape-off layer in Alcator C-Mod *J. Nucl. Mater.* **337–339** 281–5